Methodology for Modeling Non Linear Thermomechanical Response With Wear at High-Speed Interactions: Application To a Pin-Disk Configuration

Soufiane Pontonnier, Samuel Quaegebeur, Fabrice Thouverez, Patricio Almeida

Methodology for Modeling non linear Thermomechanical Response With Wear at High-Speed Interactions: Application to a Pin-Disk Configuration

S. Pontonnier[1], S. Quaegebeur[1], F.Thouverez[1], P.Almeida[2]

Abstract

An aircraft engine is a complex structure for which some components can come into contact at high speed. Modelling this behaviour is very complex as multiple physics must be considered. State-of-the-art methodologies usually account for permanent contact and thermal modelling. In this paper, a new approach is proposed and embeds various phenomena such as non-regular and non linear contact mechanics, surface rubbing, wear and non linear heat transfer. A non linear version of Moreau-Jean algorithm is employed to compute the transient response of the system and to capture accurately the contact dynamics. Moreover, the full non linear coupling between the dynamics and the heating process is taken into account through both a semi-analytical formulation and the finite-element method. At the contact interface, heat flux is generated by dry rubbing and flows into both interacting bodies. The heat flux partition is evaluated thanks to a coefficient that depends on the material properties of the solids in contact. The proposed method also accounts for the adhesive wear between the solids through an energetic approach. This methodology is applied to an academic, yet realistic, disk connected to a rotor shaft that is free to move axially and to rotate around its revolution axis. Gyroscopic effects and variation of the rotation velocity are included leading to a full non linear mechanical behaviour. The disk undergoes aerodynamic load moving it to contact with a clamped free pin. The rotor shaft and the pin are both modelled as 1D elastic bodies while the rotor disk is assumed to be rigid. Through this example, the developed strategy shows its potential to compute the complete transient highly non linear response of the breaking phenomenon, in an acceptable time simulation.

Keywords

Thermomechanics, Non linearity, Wear, High velocity, Nonregularity, Turbomachinery, Transient dynamics

1 - École Centrale de Lyon, Laboratoire de Tribologie et Dynamique des Systèmes, UMR CNRS 5513, 36 avenue Guy de Collongue, Écully, 69134, France
2 - Safran Helicopter Engines, Avenue Joseph Szydlowski, Bordes, 64510, France

Méthodologie de modélisation de la réponse thermomécanique non linéaire avec usure lors d'interactions à grande vitesse : application à une configuration pion-disque.

S. Pontonnier[1], S. Quaegebeur[1], F.Thouverez[1], P.Almeida[2]

Résumé

Un moteur d'avion est une structure complexe dans laquelle certains composants peuvent entrer en contact à grande vitesse. La modélisation de ce comportement est particulièrement exigeante car elle requiert la prise en compte de multiples phénomènes physiques. Les méthodologies présentes dans la littérature considèrent généralement l'aspect thermique du problème et se concentrent uniquement sur la phase de contact permanent. Cet article propose une nouvelle approche intégrant divers phénomènes tels que la mécanique de contact non régulière et non linéaire, le frottement de surface, l'usure et le transfert de chaleur non linéaire. Une version non linéaire de l'algorithme de Moreau-Jean est employée pour calculer la réponse transitoire du système, permettant de capturer avec précision la dynamique de contact. Le couplage entre la dynamique et le processus thermique est assuré par une formulation semi-analytique et la méthode des éléments finis. À l'interface de contact, un flux thermique généré par le frottement à sec se diffuse dans les deux corps en interaction. La répartition de ce flux est déterminée par un coefficient de partage dépendant des propriétés des matériaux en contact. La méthode prend également en compte l'usure adhésive à l'aide d'une approche énergétique. Cette méthodologie est appliquée à un cas académique mais réaliste, dans lequel un disque est connecté à l'arbre d'un rotor, libre de se déplacer axialement et de tourner autour de son axe. Les effets gyroscopiques et la variation de vitesse de rotation sont intégrés, aboutissant à un comportement mécanique non linéaire. Le disque est soumis à une charge aérodynamique le mettant en contact avec un pion encastré-libre. L'arbre du rotor et le pion sont modélisés comme des corps élastiques 1D, tandis que le disque est supposé rigide. Cet exemple illustre le potentiel de la stratégie développée pour calculer la réponse transitoire complète et fortement non linéaire du phénomène de freinage dans un temps de simulation acceptable.

Mots-clés

Thermomécanique, Non linéarités, Usure, Hautes vitesses, Turbomachines, Dynamique transitoire, Dynamique non régulière

1 - École Centrale de Lyon, Laboratoire de Tribologie et Dynamique des Systèmes, UMR CNRS 5513, 36 avenue Guy de Collongue, Écully, 69134, France
2 - Safran Helicopter Engines, Avenue Joseph Szydlowski, Bordes, 64510, France

1 Introduction

Aircraft engines are complex structures in which components operate under extreme conditions (high temperature, and rotating speeds). Braking systems are a crucial component to slow down the system. Developing appropriate tools to model the whole braking interaction may help to further improve the security and performance of aircraft engines.

In turbomachinery, this phenomena is covered by rotor/stator interaction for which the literature is abundant. The rotor can be slowed down by radial [1] or axial rubbing [2, 3, 4, 5]. The latter being the subject of the present paper, some of the most up to date studies are briefly summarized hereafter. References [2, 3, 4] have proposed a finite element (FE) methodology to model the transient interaction. Psarra [2] developed wear maps (including adhesive wear and melt) based on previously obtained FE simulation results. The author have then used this work to compute directly the wear volume of the stator interacting with the rotor. The developed tool showed good correlation with FE simulation. However, the full complexity of the melting phenomenon is not entirely represented. Besides, the dynamics of the rotor is not considered, only purely axial displacement of the rotor is considered. Capozzi et al. [3] developed a three dimensional FE model accounting for impacts and wear represented by a damage criteria. This work has then been enhanced by Rojo et al. [4] who added thermomechanical coupling. In order to decrease the computation cost of such methodology, Eryilmaz et al. [5] proposed a simple analytical model to represent the instantaneous melt of the stator interface due to rubbing with the rotor, considering linear heat equation and permanent contact.

This paper focuses on developing a semi-analytical model able to represent the system dynamics before melting occurs, with a small computation time. Predicting such behaviour is very challenging as plenty of physics is involved.

The first main challenge is to model the impacts occurring within the system. To tackle such problem, two types of numerical algorithm referred to as event-driven or event-capturing approaches [6] can be used. The former requires two methods: one to solve the free dynamics and one to solve the contact dynamics. This type of algorithm is not well suited to problems embedding many impacts, as it becomes time consuming and may not converge. In this paper, event-capturing method is preferred as it allows to solve the whole response within a single algorithm.

During the braking interaction, the second challenge is to model the friction process and its consequences. The main parameter governing the phenomena is the friction coefficient μ, which depends on external parameters such as contact pressure, sliding velocity or temperature [7, 8, 9, 10]. The results of the aforementioned references show that an increase in pressure or in sliding velocity lead to a decrease of μ, down to an asymptotic value.

As a consequence of the rubbing interaction between the solids, both wear and heat generation occur. Various models have been developed in order to quantify the wear [11], among them energy based method is shown to be very effective [12]. Early investigations on the heat generation through friction were made by [13, 14, 15] and showed that heat flux is not equally shared by the contacting bodies highlighting the need for a heat partition factor. The aforementioned references studied semi-infinite solids in perfect contact with a moving heat source and showed that the heat partition factor depends on the Peclet number and thus on the properties of the interaction.

Another approach considers that the heat division should only depends on material properties and that no difference have to be made between the moving and the fixed solid [16]. Charron and al. [17] related the heat partition factor with the thermal effusivity using semi-infinite solids and Block's postulate. Charron's formula is still being widely used, especially in studies where the interaction is transient and occurs at high relative velocity [5, 18, 19].

The methodology proposed in this work combines different methods into a single framework so that all the aforementioned physics (contact, friction, wear, and heat processes) can be included. It has been numerically implemented using Python programming language . The paper is organized as follow: Section 2 presents both the key equations to model the dynamics as well as the algorithm used to solve it. The modelling of the interface behaviour is detailed within Section 3. The developed methodology is then applied to a free rotor - fixed pin configuration explained in Section 4. Due to the complexity of the proposed approach, its full validation is complex. However, the mechanical model and its temperature evolution are validated against a finite element model, using Ansys Workbench , in Section 5. Finally, the developed methodology is employed to compute the complete system dynamics in Section 6. The influence of the thermal modelling and the wear is studied.

2 General formulation

2.1 Governing equations

In this paper, non linear thermomechanical coupling is considered. The governing system of equations is

$$\begin{cases} \mathrm{div}(\boldsymbol{\sigma}\,(T)) - \rho\ddot{\mathbf{u}} = 0, \\ \rho C_{\mathrm{p}}(T)\dfrac{\partial T}{\partial t} = \nabla_{\mathbf{x}}^{\intercal}\nabla_{\mathbf{x}}(\lambda(T)T) - \rho\dot{\mathbf{u}}^{\intercal}\nabla_{\mathbf{x}}C_{\mathrm{p}}(T)T, \end{cases} \tag{1}$$

where $\mathbf{u}$ and T are the unknowns of the system referring to the internal displacement and temperature. Appropriate initial conditions and boundary conditions have to be applied in order to solve Eq. (1). The scalars C_{p}, λ, and ρ denote the heat capacity, the thermal conductivity, and the density respectively. $\nabla_{\mathbf{x}}$ is the gradient with respect to $\mathbf{x}$ (which is here the space variables). The operator $^{\intercal}$ denotes the transpose operator. The tensor $\boldsymbol{\sigma}$ refers to the stress tensor. The first line of Eq. (1) describes the mechanical behaviour of the system while the second line gives the non linear heat conduction in the solids [20]. It should be noted that the term due to elastic deformation has been omitted in the second line of Eq. (1) as it only has significant impact on mesoscopic systems. The coupling between the two lines of Eq. (1) comes from the material properties dependence on the temperature

$$\boldsymbol{\sigma}\,(T) = \mathbf{H}(T) : [\boldsymbol{\epsilon}^{e} - \alpha_{\mathrm{thexp}}T\mathbf{I}]\,, \tag{2}$$

with $\mathbf{H}(T)$ the elasticity tensor, $\boldsymbol{\epsilon}^{e}$ the deformation tensor and α_{thexp} the thermal expansion coefficient. The matrix $\mathbf{I}$ refers to the identity matrix.

The finite element method is applied to the system given in Eq. (1) and provides

$$\tilde{\mathbf{M}}\ddot{\tilde{\mathbf{q}}} + \tilde{\mathbf{C}}\dot{\tilde{\mathbf{q}}} + \tilde{\mathbf{K}}\tilde{\mathbf{q}} = \mathbf{f}_{\mathrm{ext}} + \mathbf{f}_{\mathrm{cont}}. \tag{3}$$

The matrix $\tilde{\mathbf{K}}$ gathers the stiffness and thermal conductivity matrices as well as their coupling. A similar construction is obtained for $\tilde{\mathbf{M}}$ and $\tilde{\mathbf{C}}$ (which includes the structural damping matrix, the gyroscopic matrix and the thermal mass matrix). A full detailed example is provided in Section 4.4. The vectors $\mathbf{f}_{\mathrm{ext}}(\mathbf{q}, \dot{\mathbf{q}}, t)$ and $\mathbf{f}_{\mathrm{cont}}$ corresponds to the external load and contact forces respectively. The vector $\tilde{\mathbf{q}}$ is defined as $\tilde{\mathbf{q}} = [\mathbf{q}^{\intercal}, \mathbf{T}^{\intercal}]^{\intercal}$, where $\mathbf{q}$ denotes the mechanical degrees of freedom and $\mathbf{T}$ the thermal degrees of freedom.

2.2 Algorithm for transient non-smooth problem

The contact force in Eq. (3) must satisfy the Signorini conditions,

$$0 \leq v_{\mathrm{norm}}^{+} + e v_{\mathrm{norm}}^{-} \perp \Lambda \geq 0, \tag{4}$$

where v_{norm}^{-}, v_{norm}^{+} both represent the normal velocity before and after impact respectively. Λ is an equivalent to a Lagrange multiplier and corresponds to an impulse. Finally, e is the restitution coefficient from Newton impact law. In case of $e = 0$ there is no bounce and the contact is fully dissipative. In the opposite, $e = 1$ the contact is elastic and bounces occur.

To handle such non-linearity, Moreau-Jean algorithm [6, 21, 22] is here employed. However, its classical formulation has the drawback of presenting residual penetrations in some cases [1, 6]. A corrected formulation has been proposed in [23], and is thus used in this paper. In the present study the algorithm is further adjusted in order to account for the thermo-mechanical behavior. The following derivations give a brief description of the algorithm as well as its improvements, the reader is referred to [6] for the full detailed derivation. Eq. (3) is integrated in time providing the first line of the following system

$$\begin{cases} \int_{(t_n, t_{n+1}]} \tilde{\mathbf{M}}\mathrm{d}\mathbf{v} + \int_{t_n}^{t_{n+1}} \tilde{\mathbf{f}}\mathrm{d}t = \int_{(t_n, t_{n+1}]} \mathbf{c}_{\mathrm{N}\Lambda}\mathrm{d}\mathbf{f}_{\mathrm{cont}} \\ \tilde{\mathbf{q}}(t_{n+1}) = \int_{t_n}^{t^{n+1}} \left(\dot{\tilde{\mathbf{q}}}^{+} + \mathbf{c}_{\mathrm{N}}\gamma(t)\right)\mathrm{d}t, \end{cases} \tag{5}$$

with $\mathrm{d}\mathbf{v}$ a differential measure that provides

$$\int_{(t_n, t_{n+1}]} \tilde{\mathbf{M}}\mathrm{d}\mathbf{v} = \tilde{\mathbf{M}}\left(\dot{\tilde{\mathbf{q}}}^{+}(t_{n+1}) - \dot{\tilde{\mathbf{q}}}^{+}(t_n)\right) \tag{6}$$

and

$$\tilde{\mathbf{f}} = \tilde{\mathbf{K}}\tilde{\mathbf{q}} + \tilde{\mathbf{C}}\dot{\tilde{\mathbf{q}}} - \mathbf{f}_{\text{ext}}. \tag{7}$$

In Eq. (5), $\mathrm{d}\mathbf{f}_{\text{cont}}$ is an impulse due to the contact and $\gamma(t)$ is an added multiplier at the velocity level to ensure non residual penetration. The second line of Eq. (5) corresponds to the integration of the velocity with the added corrector providing the displacement. Vectors $\mathbf{c}_{\text{N}}$ and $\mathbf{c}_{\text{N}\Lambda}$ allow to pass from the local normal direction to the global reference frame. After performing time discretization on Eq. (5) with use of the $\theta-$method, the residual $\mathfrak{R}$ is defined as

$$\mathfrak{R} = \begin{bmatrix} \mathfrak{R}_1 \\ \mathfrak{R}_2 \end{bmatrix} = \begin{bmatrix} \tilde{\mathbf{M}}(\tilde{\mathbf{q}}_{n+\theta})(\dot{\tilde{\mathbf{q}}}_{n+1} - \dot{\tilde{\mathbf{q}}}_n) + \Delta t \tilde{\mathbf{f}}_{n+\theta} - \mathbf{p}_{n+1} \\ \tilde{\mathbf{q}}_{n+1} - \tilde{\mathbf{q}}_n - \Delta t \dot{\tilde{\mathbf{q}}}_{n+\theta} - \tau_{n+1} \end{bmatrix}, \tag{8}$$

$\mathfrak{R}$ is split into two parts: $\mathfrak{R}_1$ and $\mathfrak{R}_2$, which denote the residual in terms of dynamics and displacement. In Eq. (8), $\tilde{\mathbf{f}}_{n+\theta}$ is defined as $\tilde{\mathbf{f}}_{n+\theta} = \tilde{\mathbf{f}}(\tilde{\mathbf{q}}_{,n+\theta}, \dot{\tilde{\mathbf{q}}}_{n+\theta})$ and $\tilde{\mathbf{q}}_{n+\theta}$ is equal to $\tilde{\mathbf{q}}_{n+\theta} = \theta\tilde{\mathbf{q}}_{n+1} + (1-\theta)\tilde{\mathbf{q}}_n$. The vectors $\mathbf{p}_{n+1}$, $\boldsymbol{\tau}_{n+1}$ correspond to reaction terms in the global frame, defined as

$$\begin{cases} \mathbf{p}_{n+1} = \mathbf{c}_{\text{N}\Lambda}(\mathbf{q}_{n+1})\Lambda_{n+1} \approx \int_{(t_n, t_{n+1}]} \mathbf{c}_{\text{N}\Lambda} \mathrm{d}\mathbf{f}_{\text{cont}}, \\ \boldsymbol{\tau}_{n+1} = \mathbf{c}_{\text{N}}(\mathbf{q}_{n+1})\kappa_{n+1} = \int_{t_n}^{t^{n+1}} \mathbf{c}_{\text{N}}\gamma(t)\mathrm{d}t. \end{cases} \tag{9}$$

The system in Eq. (8) is non linear and thus a Newton-Raphson algorithm is employed to solve it. Superscript ^{i} is used to denote the i-th iteration of the algorithm. It should be pointed out that gradients of $\tilde{\mathbf{M}}$, $\mathbf{c}_{\text{N}}$ and $\mathbf{c}_{\text{N}\Lambda}$ with respect to $\tilde{\mathbf{q}}$, $\dot{\tilde{\mathbf{q}}}$ and $\mathbf{T}$ are neglected within the loop [23]. The linearization of the residue is noted $\mathfrak{R}_L$ and is equal to

$$\mathfrak{R}_L(\tilde{\mathbf{q}}^{i+1}_{n+1}, \dot{\tilde{\mathbf{q}}}^{i+1}_{n+1}) = \mathfrak{R}(\tilde{\mathbf{q}}^{i}_{n+1}, \dot{\tilde{\mathbf{q}}}^{i}_{n+1}) + \begin{bmatrix} \tilde{\mathbf{M}}(\tilde{\mathbf{q}}^i_{n+\theta}) + \Delta t\theta \mathbf{C}_\nabla \\ -\Delta t\theta \mathbf{I} \end{bmatrix} (\dot{\tilde{\mathbf{q}}}^{i+1}_{n+1} - \dot{\tilde{\mathbf{q}}}^{i}_{n+1}) + \begin{bmatrix} \Delta t\theta \mathbf{K}_\nabla \\ \mathbf{I} \end{bmatrix} (\tilde{\mathbf{q}}^{i+1}_{n+1} - \tilde{\mathbf{q}}^{i}_{n+1}). \tag{10}$$

with $\mathbf{C}_\nabla = \nabla_{\dot{\tilde{\mathbf{q}}}_{n+1}} \tilde{\mathbf{f}}^i_{n+\theta}$ and $\mathbf{K}_\nabla = \nabla_{\tilde{\mathbf{q}}_{n+1}} \tilde{\mathbf{f}}^i_{n+\theta}$. During Newton's procedure, $\mathfrak{R}_L(\tilde{\mathbf{q}}^{i+1}_{n+1}, \dot{\tilde{\mathbf{q}}}^{i+1}_{n+1})$ is taken equal to 0 in Eq. (10). Therefore, the second line provides

$$\tilde{\mathbf{q}}^{i+1}_{n+1} = \tilde{\mathbf{q}}_n + \Delta t \left(\theta \dot{\tilde{\mathbf{q}}}^{i+1}_{n+1} + (1-\theta)\dot{\tilde{\mathbf{q}}}_n \right) + \tau^{i+1}_{n+1}. \tag{11}$$

This equation is substituted into the first line of Eq. (10) and allows to express the velocity at the iteration $i+1$

$$\dot{\tilde{\mathbf{q}}}^{i+1}_{n+1} = \mathbf{v}^{i+1}_{\text{pr}} + \left(\hat{\mathbf{M}}^i \right)^{-1} \mathbf{p}^{i+1}_{n+1}, \tag{12}$$

with the iteration matrix $\hat{\mathbf{M}}^i$ equal to

$$\hat{\mathbf{M}}^i = \tilde{\mathbf{M}}(\tilde{\mathbf{q}}^i_{n+\theta}) + \Delta t\theta \mathbf{C}_\nabla + \Delta t^2 \theta^2 \mathbf{K}_\nabla. \tag{13}$$

In Eq. (12), $\mathbf{v}^{i+1}_{\text{pr}}$ is the predicted velocity defined as

$$\mathbf{v}^{i+1}_{\text{pr}} = \dot{\tilde{\mathbf{q}}}^i_{n+1} - \hat{\mathbf{M}}^{-1} \left(\boldsymbol{\delta}^i + \Delta t\theta \mathbf{K}_\nabla \boldsymbol{\tau}^i_{n+1} \right) [1] \tag{14}$$

with

$$\boldsymbol{\delta}^i = \mathfrak{R}_1(\tilde{\mathbf{q}}^i_{n+1}, \dot{\tilde{\mathbf{q}}}^i_{n+1}) + \Delta t\theta \mathbf{K}_\nabla \left(\tilde{\mathbf{q}}_n + \Delta t \dot{\tilde{\mathbf{q}}}^i_{n+\theta} - \tilde{\mathbf{q}}^i \right). \tag{15}$$

In order to detect the contact between the two solids, the gap must be evaluated. It is equal to the normal distance (along $\overrightarrow{\mathrm{X}}$) between the solids and it is defined by

$$g^{i+1} = g_0 + \mathbf{c}_{\text{N}}{}^{\intercal} \tilde{\mathbf{q}}^{i+1}_{n+1}, \tag{16}$$

[1] As in [23], the system is decoupled by considering $\boldsymbol{\tau}_{n+1}$ at the Newton iteration i rather than $i+1$.

In case of $g^{i+1} > 0$, no correction is made and $\dot{\tilde{\mathbf{q}}}_{n+1}^{i+1} = \mathbf{v}_{\mathrm{pr}}^{i+1}$. Otherwise, two linear complementarity problems (LCP) are solved [6]. The first one is written at the velocity level

$$\begin{cases} \mathbf{c}_{\mathrm{N}}{}^{\intercal}(\tilde{\mathbf{q}}_{n+1}^{i})(\dot{\tilde{\mathbf{q}}}_{n+1}^{i+1} + e\dot{\tilde{\mathbf{q}}}_{n}) = \mathbf{W}_{n+1}^{i+1}\Lambda_{n+1}^{i+1} + \mathbf{c}_{\mathrm{N}}{}^{\intercal}(\tilde{\mathbf{q}}_{n+1}^{i})(\mathbf{v}_{\mathrm{pr}}^{i+1} + e\dot{\tilde{\mathbf{q}}}_{n}) \\ 0 \leq \mathbf{c}_{\mathrm{N}}{}^{\intercal}(\tilde{\mathbf{q}}_{n+\theta}^{i})(\mathbf{v}_{\mathrm{pr}}^{i+1} + e\dot{\tilde{\mathbf{q}}}_{n}) \perp \Lambda_{n+1}^{i+1} \geq 0, \end{cases} \tag{17}$$

with $\mathbf{W}_{n+1}^{i+1} = \mathbf{c}_{\mathrm{N}}(\tilde{\mathbf{q}}_{n+1}^{i})^{\intercal}\hat{\mathbf{M}}^{-1}\mathbf{p}_{n+1}^{i+1}$. The second one in case of $\Lambda_{n+1}^{i+1} = 0$,

$$\begin{cases} g_{n+1}^{i+1} = g_{n+1}^{i} + \mathbf{c}_{\mathrm{N}}{}^{\intercal}(\tilde{\mathbf{q}}_{n+\theta}^{i})(\tilde{\mathbf{q}}_{n} + \Delta t\left(\theta\dot{\tilde{\mathbf{q}}}_{n+1}^{i+1} + (1-\theta)\dot{\tilde{\mathbf{q}}}_{n}\right) - \tilde{\mathbf{q}}_{n+1}^{i} + \mathbf{c}_{\mathrm{N}}(\tilde{\mathbf{q}}_{n+\theta}^{i})\tau_{n+1}^{i+1}) \\ 0 \leq g_{n+1}^{i+1} \perp \kappa_{n+1}^{i+1} \geq 0. \end{cases} \tag{18}$$

If $\Lambda_{n+1}^{i+1} > 0$, then κ_{n+1}^{i+1} is obtained by solving $g_{n+1}^{i+1} = 0$. The Newton loop ends when either the absolute or relative residual verify

$$\begin{cases} \dfrac{\left\|\mathfrak{R}(\tilde{\mathbf{q}}_{n+1}^{i+1}, \dot{\tilde{\mathbf{q}}}_{n+1}^{i+1})\right\|}{\left\|\mathbf{p}_{n+1}^{i+1}\right\|} \leq 10^{-4} \\ \text{or} \\ \left\|\mathfrak{R}(\tilde{\mathbf{q}}_{n+1}^{i+1}, \dot{\tilde{\mathbf{q}}}_{n+1}^{i+1})\right\| \leq 10^{-10}. \end{cases} \tag{19}$$

2.2.1 Tangent matrices

To compute the predicted velocity (see Eq. (14)), terms $\mathbf{K}_{\nabla}$ and $\mathbf{C}_{\nabla}$ must be evaluated, in the present paper they are equal to

$$\begin{cases} \mathbf{K}_{\nabla} = \tilde{\mathbf{K}}^{i} + \nabla_{\tilde{\mathbf{q}}_{n+1}}\left(\tilde{\mathbf{K}}^{i}\right)\tilde{\mathbf{q}}_{n+\theta}^{i} + \nabla_{\tilde{\mathbf{q}}_{n+1}}\left(\tilde{\mathbf{C}}^{i}\right)\dot{\tilde{\mathbf{q}}}_{n+\theta}^{i} \\ \\ \mathbf{C}_{\nabla} = \nabla_{\dot{\tilde{\mathbf{q}}}_{n+1}}\left(\tilde{\mathbf{C}}^{i}\right)\dot{\tilde{\mathbf{q}}}_{n+\theta}^{i} + \tilde{\mathbf{C}}^{i} + \nabla_{\dot{\tilde{\mathbf{q}}}_{n+1}}\left(\tilde{\mathbf{K}}^{i}\right)\tilde{\mathbf{q}}_{n+\theta}^{i} - \nabla_{\dot{\tilde{\mathbf{q}}}_{n+1}}\mathbf{f}_{\mathrm{ext},n+\theta}^{i}. \end{cases} \tag{20}$$

3 Modeling of the contact interface

When two solids are in contact with a relative velocity, a friction force $\mathbf{f}_{\mathrm{T}}$, opposed to the movement, is generated. Coulomb law is widely used [10] for macro-modeling and is here employed. During sliding, the tangent force is given by

$$\mathbf{f}_{\mathrm{T}}(t) = -\mu f_{\mathrm{N}}(t)\frac{\mathbf{v}_{\mathrm{g}}(t)}{\|\mathbf{v}_{\mathrm{g}}(t)\|}, \tag{21}$$

with f_{N} the normal force due to contact and $\mathbf{v}_{\mathrm{g}}$ the sliding velocity. f_{N} is greater than 0 in case of contact and null otherwise. The notation $\|\cdot\|$ stands for the L_2 norm. In order to simplify the present study, the friction coefficient has been assumed constant with $\mu = 0.1$. This value is frequently found in the literature for materials made of inconel 718 ([2, 24]) . This friction process leads to two main phenomena: wear and heat generation whose modeling in the proposed method is detailed next.

3.1 Adhesive wear

The rubbing between the solids damages the contact interface by ripping adhesive joints created between contacting surface asperities [25]. It is modelled in this paper with an energetic formulation [12]. The wear depth L_{w} is assumed to evolve linearly with the dissipated energy at the interface

$$\dot{L}_{\mathrm{w}} = \kappa_{\mathrm{En}}\mu p_{\mathrm{N}}(t)\|\mathbf{v}_{\mathrm{g}}(t)\|, \tag{22}$$

where $p_{\mathrm{N}}(t)$ denotes the normal contact pressure. This formulation allows to account for variation in the contact pressure and in the friction coefficient. Also, the coefficient κ_{En} only depends on the material in contact. This methodology has been used in [12, 26] for a fretting process.

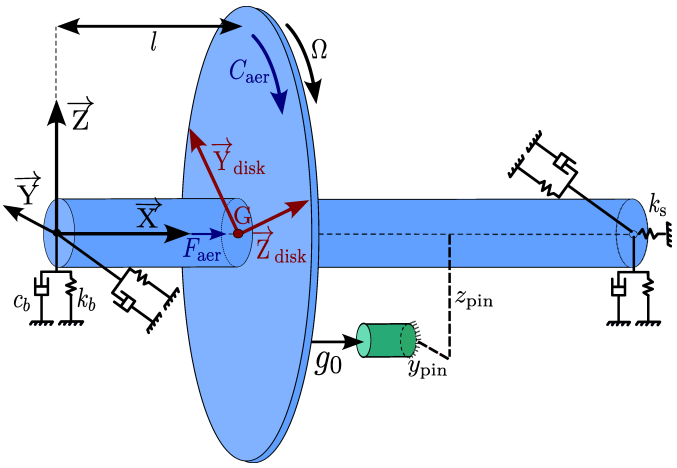

Figure 1. Studied configuration.

3.2 Heat flux generation

Energetic balance at the interface under rubbing and wear has been expressed in [27] with the use of Clausius-Duhem equation

$$\left(\dot{L}_{\mathrm{w}} p_{\mathrm{N}} + p_{\mathrm{T}} \|\mathbf{v}_{\mathrm{g}}\|\right) + \mathbf{q}_{\mathrm{cont}}^{\intercal} \mathbf{n}_{\mathrm{cont}} = 0 \tag{23}$$

where p_{T} is the tangential pressure. Also, $\mathbf{q}_{\mathrm{cont}}^{\intercal} \mathbf{n}_{\mathrm{cont}} = \mathbf{q}^{s1} \mathbf{n}^{s1} + \mathbf{q}^{s2} \mathbf{n}^{s2}$, with $\mathbf{q}^{sk}$ being the flux in solid ^{sk} while getting closer to the contact interface Γ_{cont}. The final expression of the heat flux generated at Γ_{cont} is obtained by substituting Eq. (22) in Eq. (23)

$$\mathbf{q}_{\mathrm{cont}}^{\intercal} \mathbf{n}_{\mathrm{cont}} = -\left(\kappa_{\mathrm{En}} p_{\mathrm{N}} + 1\right) \mu p_{\mathrm{N}} \|\mathbf{v}_{\mathrm{g}}\|. \tag{24}$$

Due to the roughness of the interacting surfaces, thermal contact is not perfect and a temperature discontinuity across the contact interface exists [28]. However, the thermal conduction is limited by a thermal contact resistance. This parameter decreases with contact pressure, temperature, surface roughness [29] or sliding velocity [30, 31]. In the present study, it is assumed that the thermal resistance is low enough so that the temperature difference is negligible. This assumption is also relevant as the heat flux produced by friction reaches very high values. Thus, the overall heat flux entering the bodies is expressed as

$$\begin{cases} q^{s1} = \alpha q_{\mathrm{cont}}, \\ q^{s2} = (1-\alpha) q_{\mathrm{cont}}. \end{cases} \tag{25}$$

In Eq. (25), α refers to the heat partition factor. Under the assumption of short transient interaction [32], it is obtained by Charron's formula

$$\alpha = \frac{\xi^{s1}(T^{s1})}{\xi^{s1}(T^{s1}) + \xi^{s2}(T^{s2})}, \tag{26}$$

with $\xi^{sk} = \sqrt{\rho C_{\mathrm{p}}(T^{sk}) \lambda(T^{sk})}$. Notice that the dependency of ξ on the temperature allows to model the progressive temperature disymetry in the contact [32].

4 Application to a pin-rotor disk configuration

4.1 Configuration of interest

The methodology proposed in Sections 2 and 3 is now employed on a pin-rotor configuration presented in Fig.1. It is composed of a rotor free to move axially and a clamped pin distant from the rotor disk by a distance g_0 (initial gap).

The rotor is supposed to be supported by bearings at its extremities modelled by dampers and springs along the $\overrightarrow{\mathrm{Y}}$ and $\overrightarrow{\mathrm{Z}}$ directions. They are respectively equal to c_b and k_b. The rotor shaft is free to move axially, leading to ill-conditioned matrices. To avoid this problem, a spring k_s of $10\,\mathrm{N{\cdot}m^{-1}}$ is added along $\overrightarrow{\mathrm{X}}$ at the rear extremity of the shaft. The value of the spring stiffness is chosen small enough to not disturb the system dynamics . The pin and the rotor shaft are assumed to be elastic bodies whereas the rotor disk is purely rigid and rotates at a varying speed Ω with an initial speed Ω_0. Constant aerodynamic loads are applied to the rotor. They are composed of an axial force $\mathbf{F}_\mathrm{aer}$ which brings the rotor into contact with the pin and a driving torque $\mathbf{C}_\mathrm{aer}$ which accelerates the rotor disk. Inconel 718 is used for the rotor and the pin. Material properties are taken from [33, 34]. The value for κ_En in Eq. (22) is equal to $\kappa_\mathrm{En} = 11.31 \cdot 10^{-9}\,\mathrm{MPa}^{-1}$. It corresponds to the mean value provided in Tab.6 for untreated inconel 718 in [35]. The rest of the data are available in Tables 1 and 2.

Part	Length (mm)	Outter radius (mm)	Inner radius (mm)
Shaft	110	20	–
Disk	30	80	20
Pin	18	9	–

Table 1. Geometric properties.

$\mathbf{F}_\mathrm{aer}$ (N)	$\mathbf{C}_\mathrm{aer}$ (Nm)	g_0 (mm)	l (mm)
1500	20	1	60
Ω_0 (RPM)	k_b ($\mathrm{Nm^{-1}}$)	c_b ($\mathrm{Nm^{-1}s^{-1}}$)	$(y_\mathrm{pin}, z_\mathrm{pin})$ (mm)
20000	10^7	10^2	$(28, -28)$

Table 2. Complementary data.

4.2 Non linear thermomechanical behavior of the pin

4.2.1 Non linear thermal equation

The heat equation presented in Eq. (1) is applied to the pin, neglecting the term $\rho\dot{\mathbf{u}}^\intercal\nabla_\mathbf{x}C_\mathrm{p}(T)T$. Due to the rotating air in the boundary layer of the disk, the pin is submitted to forced convection modeled by a heat loss term. The 1D-non linear heat equation in the pin is written as

$$\rho C_\mathrm{p}(T)\frac{\partial T(x,t)}{\partial t} = \frac{\partial}{\partial x}(\lambda(T)\frac{\partial T(x,t)}{\partial x}) - \frac{2h_\mathrm{pin}}{r_\mathrm{pin}}T(x,t), \tag{27}$$

with h_pin the convective coefficient applied on the pin [2]. Material properties are obtained from [33] and interpolated in the temperature range $[298\,\mathrm{K}, 1{,}400\,\mathrm{K}]$. Temperature dependent material properties are assumed to follow a polynomial expansion. Based on material data [33], the following expressions are obtained

$$\begin{cases} C_\mathrm{p}(T) = 359.34 + 0.22 \times T \\ \lambda_\mathrm{pin} = 3.17 + 0.023 \times T - 4.9 \times 10^{-6} \times T^2 \end{cases} \tag{28}$$

The finite element formulation of Eq. (27) gives

$$\mathbf{C}_\mathrm{th}(\mathbf{T})\dot{\mathbf{T}} + (\mathbf{K}_\mathrm{th}(\mathbf{T}) + \mathbf{K}_\mathrm{cv}(\mathbf{q}_\mathrm{pin}, \Omega))\,\mathbf{T} = \mathbf{0}, \tag{29}$$

[2] Modeling of h_pin is presented in Appendix A

where $\mathbf{C}_{\text{th}}$ is the thermal matrix of the pin and $\mathbf{K}_{\text{th}}$ stands for the thermal conductivity matrix. The associated boundary conditions are

$$\begin{cases} T(L,t) = 0 \\ \dfrac{\partial T(0,t)}{\partial x} = \begin{cases} -\dfrac{\alpha q_{\text{cont}}}{\lambda_{\text{pin}}} \text{ if } g = 0, \\ 0 \text{ otherwise.} \end{cases} \end{cases} \tag{30}$$

4.2.2 Non linear mechanical equation

The finite element method is applied to the pin which is modeled as an 1D truss. Thus, from Eq. (1) the following system is obtained

$$\mathbf{M}_{\text{pin}}\ddot{\mathbf{q}}_{\text{pin}} + \mathbf{C}_{\text{pin}}\dot{\mathbf{q}}_{\text{pin}} + \mathbf{K}_{\text{pin}}(\mathbf{T})\mathbf{q}_{\text{pin}} + \mathbf{K}_{\alpha_{\text{thexp}}}(\mathbf{T})\mathbf{T} = \mathbf{0}, \tag{31}$$

where $\mathbf{M}_{\text{pin}}$, $\mathbf{C}_{\text{pin}}$, and $\mathbf{K}_{\text{pin}}$ denote the mass, damping, and stiffness matrices of the pin respectively. The matrix $\mathbf{K}_{\alpha_{\text{thexp}}}(\mathbf{T})$ denotes the thermal expansion matrix of the pin. The vector $\mathbf{q}_{\text{pin}}$ corresponds to the mechanical degrees of freedom of the pin. The stiffness matrix is temperature dependent as the Young modulus is approximated with a second order polynomial function of T using data from [34]. Similarly, $\mathbf{K}_{\alpha_{\text{thexp}}}(\mathbf{T})$ is assumed to be a linear function of T ([33]). In the considered range of temperature, their mean values are respectively 160 GPa and $17 \cdot 10^{-6}\,\text{K}^{-1}$.

In the present work, a modal damping approach has been chosen with a modal damping of $\xi = 3\%$. To better account for aerodynamic loads, mass damping approach seems to be more suited as mentioned in [2, 3].

If the gap is closed the pin undergoes a contact force f_{N}. The coupled dynamics of the pin behavior is described by

$$\begin{bmatrix} \mathbf{M}_{\text{pin}} & \mathbf{0} \\ \mathbf{0} & \mathbf{0} \end{bmatrix} \ddot{\mathbf{q}}_2 + \begin{bmatrix} \mathbf{C}_{\text{pin}} & \mathbf{0} \\ \mathbf{0} & \mathbf{C}_{\text{th}}(\mathbf{T}) \end{bmatrix} \dot{\mathbf{q}}_2 + \begin{bmatrix} \mathbf{K}_{\text{pin}} & \mathbf{K}_{\alpha_{\text{thexp}}} \\ \mathbf{0} & \mathbf{K}_{\text{th}}(\mathbf{T}) \end{bmatrix} \mathbf{q}_2 = \begin{bmatrix} \mathbf{f}_{\text{cont}} \\ \alpha q_{\text{cont}} \end{bmatrix} \tag{32}$$

where $\mathbf{q}_2 = [\mathbf{q}_{\text{pin}}{}^{\intercal}, \mathbf{T}^{\intercal}]^{\intercal}$.

4.3 Equation of motion and thermal conduction in the free rotor

4.3.1 Mechanical equations of the free rotor

A disk is attached to the shaft at the point noted G, distant by a length l from the shaft extremity, see Fig. 1. In the following, $R_0 = (O, \vec{\text{X}}, \vec{\text{Y}}, \vec{\text{Z}})$ denotes the global fixed reference frame where the shaft is defined, and $R = (G, \vec{\text{x}}_{\text{disk}}, \vec{\text{y}}_{\text{disk}}, \vec{\text{z}}_{\text{disk}})$ describes the moving reference frame attached to the disk center. In order to express the motion from R_0 to R, Euler angles are employed: a precession ψ around $\vec{Z}$, followed by a nutation θ around $\vec{\text{y}}_1$, and finally a rotation ϕ around $\vec{\text{x}}_{\text{disk}}$. Therefore two intermediate frames are defined ($R_1 = (G, \vec{\text{x}}_1, \vec{\text{y}}_1, \vec{\text{z}}_1)$ and $R_2 = (G, \vec{\text{x}}_2, \vec{\text{y}}_2, \vec{\text{z}}_2)$) to shift from R_0 to R. The angles ψ and θ are assumed to be small whereas $\dot{\phi}$ corresponds to the rotating speed of the system. In the following, ψ and θ are noted θ_z and θ_y. The vector of rotation of the disk (expressed in the frame R) is then given by

$$\boldsymbol{\omega} = \begin{bmatrix} \omega_x \\ \omega_y \\ \omega_z \end{bmatrix} = \begin{bmatrix} \dot{\phi} - \theta_y\dot{\theta}_z \\ \dot{\theta}_z \sin\phi + \dot{\theta}_y \cos\phi \\ \dot{\theta}_z \cos\phi - \dot{\theta}_y \sin\phi \end{bmatrix}. \tag{33}$$

Fig. 2 summarizes the motion of the disk. The rotor has a rigid motion around $\vec{\text{x}}_{\text{disk}}$ parameterized by the angle ϕ.

The disk, of mass m and of moments of inertia (J_{x}, J, J) along the main axis of R, is assumed to be a rigid body and is thus only characterized by its kinetic energy:

$$Ec_{\text{disk}} = \frac{1}{2}m\left(\dot{u}_G^2 + \dot{v}_G^2 + \dot{w}_G^2\right) + J_{\text{x}}\left(\dot{\phi}^2 - 2\theta_{y,G}\dot{\theta}_{z,G}\dot{\phi}\right) + J\left(\dot{\theta}_{y,G}^2 + \dot{\theta}_{z,G}^2\right). \tag{34}$$

The scalars u_G, v_G, w_G, $\theta_{y,G}$, and $\theta_{z,G}$ denote the translations and rotations of the point G (where the disk is attached to). The rotor shaft (of length L and section S) is modeled using Timoshenko beam theory. The computation of its kinetic energy is performed similarly as the disk and is given by [36]

$$Ec_{\text{shaft}} = \frac{1}{2}\rho S \int_0^L \left(\dot{u}^2 + \dot{v}^2 + \dot{w}^2 + I_G\omega_x^2 + I\left(\omega_y^2 + \omega_z^2\right)\right) \mathrm{d}x, \tag{35}$$

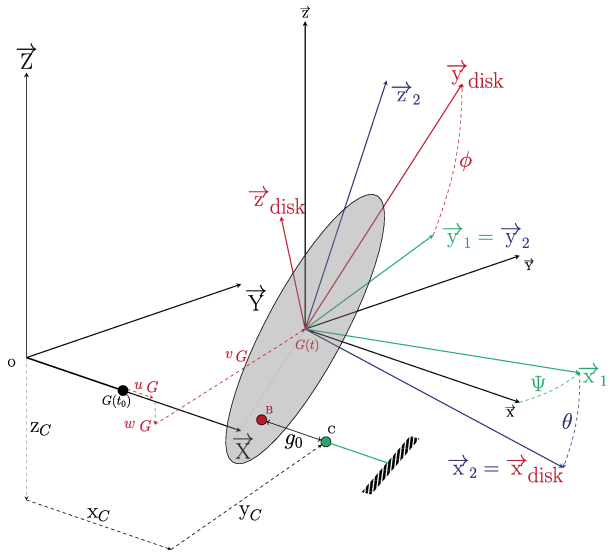

Figure 2. Frame systems used in the present paper.

where u, v, w, ω_x, ω_y, and ω_z are the translation and rotation of an arbitrary point of the neutral axis. The moments of inertia of the shaft along the main axis of R are noted (I_G, I, I). The potential energy is given [36] by

$$E_p = \frac{1}{2}\int_0^L \left(EI\left[\left(\frac{\partial \theta_y}{\partial x}\right)^2 + \left(\frac{\partial \theta_z}{\partial x}\right)^2\right] + \kappa_{\mathrm{Tim}} GS\left[\left(\frac{\partial w_s}{\partial x}\right)^2 + \left(\frac{\partial v_s}{\partial x}\right)^2\right] + ES\left(\frac{\partial u}{\partial x}\right)^2 \right) \mathrm{d}x, \tag{36}$$

where κ_{Tim} is the shear coefficient whose value is provided in [37], which here is equal to 0.85. In Eq. (36) the subscript $_s$ stands for the shear component of the total displacement. The finite element method is next applied, the shape functions used in this paper are modified Hermitian polynomials [36]. A node (G) is created where the disk is attached to. The mechanical degrees of freedom of the rotor are written $\mathbf{q}_{\mathrm{rot}}$. This vector of unknowns also contains the unknown ϕ which governs the rotation evolution of the system along $\vec{X}$. The final equation of motion of the rotor reads

$$\mathbf{M}_{\mathrm{rot}}\ddot{\mathbf{q}}_{\mathrm{rot}} + \mathbf{C}_{\mathrm{rot}}\dot{\mathbf{q}}_{\mathrm{rot}} + \mathbf{K}_{\mathrm{rot}}\mathbf{q}_{\mathrm{rot}} = \mathbf{f}_{\mathrm{rot}} + \mathbf{f}_{\mathrm{cont}}. \tag{37}$$

The terms $\mathbf{M}_{\mathrm{rot}}$, $\mathbf{C}_{\mathrm{rot}}$, and $\mathbf{K}_{\mathrm{rot}}$ denote the mass, damping (with a 3% modal damping), and stiffness matrices respectively. Notice that the stiffness and damping values of the bearings (k_{b} and c_{b}) are included in $\mathbf{K}_{\mathrm{rot}}$ and $\mathbf{C}_{\mathrm{rot}}$. The gyroscopic matrix, arising from term $I_G\omega_x^2$ in Eq. (35), is included in the damping matrix. Similarly, the angular acceleration matrix coming from the same term in Eq. (35) is included within the mass matrix as ϕ is unknown.

4.3.2 Analytic solution for thermal conduction in the rotor disk

In order to assess the temperature in the rotating rigid disk, an analytic solution of Eq. (1) is used. Arizmendi et al. [38] extended the solution of [39] to transient regime by employing successively a Fourier transform, a Hankel transform and a modal projection for which the temperature is noted T_{M}. They considered several disk configurations with constant Ω submitted to a constant heat source. In the present paper, the interaction is assumed to be very short, thus heat does not have enough time to diffuse out of the contact area and temperature at the edges is

assumed to remain constant. The configuration retained for the present paper is described by

$$\begin{cases} T(r_{\text{disk}},\varphi,x,t)=0, \\ T(r,\varphi,0,t)=0, \\ -\dfrac{\partial T(r,\varphi,e_{\text{disk}})}{\partial x} = \begin{cases} -\dfrac{q(r,\varphi,t)}{\lambda} \text{ in the contact area,} \\ h_{\text{disk}} T(r,\varphi,e_{\text{disk}},t) \text{ elsewhere,} \end{cases} \end{cases} \tag{38}$$

with e_{disk} the disk thickness. The rotation velocity and the heat source are time dependent, the second line of Eq. (1) is transformed using Fourier, Hankel and modal transform. The resulting equation is then time discretized with use of the $\theta-$method leading to

$$T_{\text{M},n+1}(\xi_m,j,\eta_p,t) = \frac{1}{\theta\Delta t\kappa\zeta_{n+1}+1}\left(\frac{\Delta t\kappa\sin\eta_p e_{\text{disk}}}{\lambda} q_{\text{H},n+1}(\xi_m,j,t) - \left[(1-\theta)\Delta t\kappa\zeta_{n+1}-1\right] T_{\text{M},n}(\xi_m,j,\eta_p,t)\right) \tag{39}$$

with $\zeta=\xi_m^2+\mathrm{i}j\dfrac{\Omega}{\kappa}+\eta_p^2$ and ξ_m, η_p the positive roots of

$$\begin{cases} J_n(\xi_m r_{\text{disk}})=0, \\ \eta_p\cot(\eta_p e_{\text{disk}}) = -h_{\text{disk}}. \end{cases} \tag{40}$$

The temperature $T(r,\varphi,x,t)$ is obtained with

$$T(r,\varphi,x,t_{n+1}) = \text{Re}\left(\sum_{j=0}^{\infty}\sum_{m=0}^{\infty}\sum_{p=0}^{\infty}\frac{R_{\text{H}}(\xi_m,r)}{N_{\text{H}}(\xi_m)}\frac{\Psi_{\text{M}}(\eta_p,x)}{N_{\text{M}}(\eta_p)} T_{\text{M},n+1} e^{ij\varphi}\right). \tag{41}$$

Transformation functions were obtained in [40] and q_{H} is the transformed heat flux as defined in [41]. In the particular case of $j>0$ and $m=0$, $q_{\text{H}}(\xi_0,j,t)=0$.

As mentioned in Section 3.2, the temperatures of both contacting solids change the heat partition factor. Thus, evaluating Eq. (41) at the coordinate $(r_{\text{pin}}, -\text{atan}(\frac{R_{\text{pin}}}{r_{\text{pin}}}), e_{\text{disk}})$, enables to compute the temperature at the entrance of the contact area.

4.4 Overall system of equation and application of the Moreau-Jean algorithm

The entire test case has now been described and the equations governing the dynamics of the pin Eq. (32) and the rotor Eq. (37) are gathered following the construction of Equation Eq. (3) to apply Moreau-Jean algorithm. As a reminder, the system of equations reads

$$\tilde{\mathbf{M}}\ddot{\tilde{\mathbf{q}}} + \tilde{\mathbf{C}}\dot{\tilde{\mathbf{q}}} + \tilde{\mathbf{K}}\tilde{\mathbf{q}} = \tilde{\mathbf{f}}. \tag{42}$$

The vector $\tilde{\mathbf{q}}$ gathers the mechanical degrees of freedom of the pin and the rotor but also the temperature degrees of freedom of the pin and is thus equal to

$$\tilde{\mathbf{q}} = \begin{bmatrix} \mathbf{q}_{\text{rot}}{}^{\intercal} & \mathbf{q}_{\text{pin}}{}^{\intercal} & \mathbf{T}^{\intercal} \end{bmatrix}^{\intercal}. \tag{43}$$

The others terms, i.e., $\tilde{\mathbf{M}}$, $\tilde{\mathbf{C}}$, $\tilde{\mathbf{K}}$, and $\tilde{\mathbf{f}}$ are similarly constructed. Recall that the temperature of the disk is considered analytically through Eq. (41).

To apply the Moreau-Jean algorithm, it then remains to define the projection vectors $\mathbf{c}_{\text{N}}$ and $\mathbf{c}_{\text{N}\Lambda}$ (Eq. (9)). The vector $\mathbf{c}_{\text{N}}$ is obtained through the derivation of the gap, i.e. the normal distance between the rotor surface and the pin surface, which is detailed hereafter. The contacting point belonging to the disk surface ($\mathfrak{S}_{\text{disk}}$) is noted B (see Fig. 2) and is assumed to be, for all time t, the normal projection of the pin extremity on $\mathfrak{S}_{\text{disk}}$. Point B is defined in the frame of reference R_2

$$\mathbf{b}_2 = \begin{bmatrix} 0 & y_B & z_B \end{bmatrix}^{\intercal}. \tag{44}$$

Using the projection matrix $\mathbf{P}_{20}$ between the frames of reference R_2 and R_0

$$\mathbf{P}_{20} = \begin{bmatrix} 1 & -\theta_{z,\mathrm{G}} & \theta_{y,\mathrm{G}} \\ \theta_{z,\mathrm{G}} & 1 & 0 \\ -\theta_{y,\mathrm{G}} & 0 & 1 \end{bmatrix}, \tag{45}$$

point B is expressed in the reference frame through

$$\mathbf{b}_{\mathrm{ref}} = \begin{bmatrix} -\theta_{z,\mathrm{G}} y_B + \theta_{y,\mathrm{G}} z_B + (l + u_G) \\ y_{\mathrm{pin}} \\ z_{\mathrm{pin}} \end{bmatrix} \tag{46}$$

with $y_{\mathrm{pin}} = y_B + v_G$ and $z_{\mathrm{pin}} = z_B + w_G$.
The pin extremity is denoted by point C and is defined in the reference frame through

$$\mathbf{c}_{\mathrm{ref}} = \begin{bmatrix} l + g_0 + u_{\mathrm{pin}} & y_{\mathrm{pin}} & z_{\mathrm{pin}} \end{bmatrix}^{\intercal}. \tag{47}$$

Therefore the gap is equal to the projection of $(\mathbf{c}_{\mathrm{ref}} - \mathbf{b}_{\mathrm{ref}})^{\intercal}$ along the $\vec{X}$ axis,

$$\begin{aligned} g &= g_0 + y_B \theta_{z,\mathrm{G}} - z_B \theta_{y,\mathrm{G}} - u_G + u_{\mathrm{pin}} \\ &= g_0 + \mathbf{c}_{\mathrm{N}}{}^{\intercal} \tilde{\mathbf{q}}. \end{aligned} \tag{48}$$

$\mathbf{c}_{\mathrm{N}}$ is a vector of a length equal to the total number of degrees of freedom of the system, it is filled with zeros except for the node where the disk is attached and for the node of the pin where the contact occurs. For point G and point C, $\mathbf{c}_{\mathrm{N}}$ is equal to

$$\begin{aligned} \mathbf{c}_{\mathrm{N|G}} &= \begin{bmatrix} -1 & 0 & 0 & -z_B & y_B \end{bmatrix}^{\intercal} \\ \mathbf{c}_{\mathrm{N|C}} &= \begin{bmatrix} 1 & 0 & 0 & 0 & 0 \end{bmatrix}^{\intercal}. \end{aligned} \tag{49}$$

The vector $\mathbf{c}_{\mathrm{N}\Lambda}$ is obtained through the derivation of the reaction forces. The relative velocity between the rotor disk and the pin is obtained in the reference frame through

$$\mathbf{v}_{\mathrm{rel}} = \mathbf{v}_G - \mathbf{v}_C + \mathbf{P}_{20} \mathbf{P}_{2\mathrm{G}}^{-1} \left(\mathbf{\Omega} \mathbf{P}_{2\mathrm{G}} \mathbf{g}\mathbf{b} \right), \tag{50}$$

with

$$\mathbf{P}_{2\mathrm{G}} = \begin{bmatrix} 1 & 0 & 0 \\ 0 & \cos\phi & \sin\phi \\ 0 & -\sin\phi & \cos\phi \end{bmatrix},$$

and $\mathbf{\Omega}$ corresponds to the rotation matrix associated to the rotation vector ω, see Eq. (33). Thus relative velocity components along $\vec{Y}$ and $\vec{Z}$ are expressed by

$$\begin{cases} v_{\mathrm{rel},Y} = \theta_{\mathrm{G},z} (\dot{\theta}_{\mathrm{G},y} z_B - \dot{\theta}_{\mathrm{G},z} y_B) - \Omega z_B, \\ v_{\mathrm{rel},Z} = -\theta_{\mathrm{G},y} (\dot{\theta}_{\mathrm{G},y} z_B - \dot{\theta}_{\mathrm{G},z} y_B) + \Omega y_B. \end{cases} \tag{51}$$

The vector $\mathbf{c}_{\mathrm{N}\Lambda}$ refers to reaction forces, it is obtained considering efforts acting on G in the reference frame

$$\begin{cases} \mathbf{f}_{\mathrm{cont|G}} = \begin{bmatrix} -f_{\mathrm{N}} & f_{\mathrm{T},y} & f_{\mathrm{T},z} \end{bmatrix}^{\intercal}, \\ \mathbf{c}_{\mathrm{cont|G}} = \begin{bmatrix} y_B f_{\mathrm{T},z} - z_B f_{\mathrm{T},y} \\ -f_{\mathrm{N}} z_B - f_{\mathrm{T},z} \left(\theta_{\mathrm{G},y} z_B - \theta_{\mathrm{G},z} y_B \right) \\ f_{\mathrm{N}} y_B + f_{\mathrm{T},y} \left(\theta_{\mathrm{G},y} z_B - \theta_{\mathrm{G},z} y_B \right) \end{bmatrix}. \end{cases} \tag{52}$$

$\mathbf{f}_{\text{cont}|\text{G}}$ corresponds to forces acting on the translations degrees of freedom of the rotor disk and $\mathbf{c}_{\text{cont}|\text{G}}$ denotes the torques acting on the rotations. $\mathbf{c}_{\text{N}\Lambda}$ is structured in the same way than $\mathbf{c}_{\text{N}}$ thus

$$\begin{aligned}
\mathbf{c}_{\text{N}\Lambda|\text{G}} &= \begin{bmatrix} -1 \\ -\mu \dfrac{v_{\text{rel},Y}}{\|\mathbf{v}_{\text{rel}}\|} \\ -\mu \dfrac{v_{\text{rel},Z}}{\|\mathbf{v}_{\text{rel}}\|} \\ -z_B + \mu \dfrac{v_{\text{rel},Z}}{\|\mathbf{v}_{\text{rel}}\|} \left(\theta_{\text{G},y} z_B - \theta_{\text{G},z} y_B\right) \\ y_B - \mu \dfrac{v_{\text{rel},Y}}{\|\mathbf{v}_{\text{rel}}\|} \left(\theta_{\text{G},y} z_B - \theta_{\text{G},z} y_B\right) \end{bmatrix}, \\
\mathbf{c}_{\text{N}\Lambda|\text{C}} &= \begin{bmatrix} 1 & 0 & 0 & 0 & 0 \end{bmatrix}^{\intercal}
\end{aligned} \tag{53}$$

and $\mathbf{c}_{\text{N}\Lambda|\phi} = y_B f_{\text{T},z} - z_B f_{\text{T},y}$. Moreover, the line corresponding to the pin's temperature at point C is equal to $\mathbf{c}_{\text{N}\Lambda|T_{\text{C}}} = \mu \|\mathbf{v}_{\text{rel}}\|$.
Algorithm 1 summarizes the Moreau-Jean algorithm steps applied to the pin-disk test case to obtain its transient response with friction, impacts, adhesive wear, and non-linear thermal conduction. It can be noticed that wear depth is computed after solving the contact [24], the removed length is added to g_0.

5 Validation of the methodology

The proposed methodology models various complex phenomena. Therefore a full validation of the method is very challenging. Nevertheless, this section proposes partial validation of the approach and the studied configuration. First the model is validated through the comparison of the evolution of the first four bending frequencies of the rotor with respect to the rotational speed. The rotor has been discretized with the finite elements method using 10 elements. Results have been compared with those from an Ansys model composed of an 1D dimensional beam with a concentrated mass and bearings supports. Material properties given in [34] were used. Frequencies obtained with both models are displayed in Fig.3. Results match very well confirming the validity of the rotor modeling.

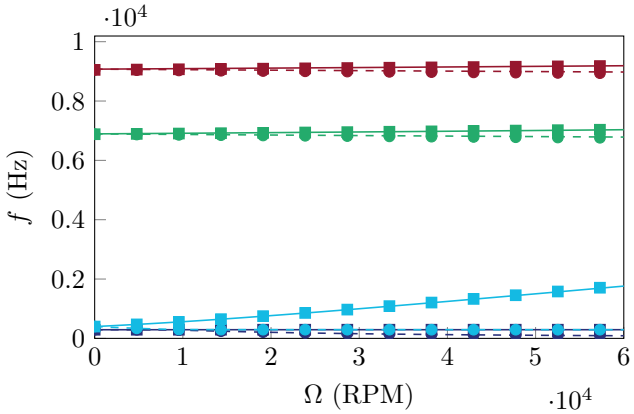

Figure 3. First bending frequencies of the supported rotor, Ansys (●)(■), Developed method (—) (- -), Forward Whirl (—)(■), Backward Whirl (- -)(●), f_1 (■), f_2 (■), f_3 (■),f_4 (■).

The pin has been discretized with 29 elements non regularly spaced. Close to the contact interface where the temperature gradient is steep, a denser mesh is used up to the distance d defined as

$$d = 3.21111\sqrt{\kappa_{\max} t_{\text{cont}}}. \tag{54}$$

Algorithm 1 Algorithm used to solve rotor disk-pin interaction, single point interaction.

while $t_n < t_{\max}$ **do**
  Update $\mathfrak{R}^0_{n+1}$ Eq. (10)
  Initialization of the array for handling contact
  $\Gamma \leftarrow$[True, False], $i \leftarrow 1$
  while Eq. (19) not satisfied or $\Gamma^i \neq \Gamma^{i-1}$ **do**
    Update $\tilde{\mathbf{f}}^{i+1}_{n+\theta}$
    Compute tangent matrices at $n+\theta \leftarrow$ Eq. (20)
    Compute $\hat{\mathbf{M}}^{i+1}_{n+\theta} \leftarrow$ Eq. (13)
    $\mathbf{v}_p \leftarrow$ Eq. (14)
    if $\Gamma^i =$ True **then**
      Solve contact
      $\Lambda^{i+1}_{n+1} \leftarrow$ Eq. (17), $\dot{\tilde{\mathbf{q}}}^{i+1}_{\text{tot},n+1} \leftarrow$ Eq. (12)
      if $\Lambda^{i+1}_{n+1} = 0$ **then** $\kappa^{i+1}_{n+1} \leftarrow$ Eq. (18)
      else if $\Lambda^{i+1}_{n+1} > 0$ **then** $\kappa^{i+1}_{n+1} \leftarrow g^{i+1}_{n+1} = 0$
      end if
      $\tilde{\mathbf{q}}^{i+1}_{n+1} \leftarrow$ Eq. (11)
    end if
    Check error Eq. (19)
    Check gap value$g^{i+1}_{n+1} \leftarrow$ Eq. (16)
    if $g^{i+1}_{n+1} \leq 0$ **then** $\Gamma^{i+1} \leftarrow$ True
    else $\Gamma^{i+1} \leftarrow$ False
    end if
    $i = i + 1$
  end while
  Update values
  $\tilde{\mathbf{q}}_{\text{tot},n+1}, \dot{\tilde{\mathbf{q}}}_{\text{tot},n+1} \leftarrow \tilde{\mathbf{q}}^{i+1}_{\text{tot},n+1}, \dot{\tilde{\mathbf{q}}}^{i+1}_{\text{tot},n+1}$
  $R_{\text{cont},n+1} \leftarrow \frac{\Lambda^{i+1}_{n+1}}{\Delta t}$
  Compute wear depth
  if $R_{\text{cont},n+1} \neq 0$ **then** $l_{\text{wear},n+1} \leftarrow$ Eq. (22)
  end if
  Compute the temperature of the disk
  $T_{\text{disk},n+1} \leftarrow$ Eq. (41)
  Update heat partition coefficient
  $\alpha_{n+1} \leftarrow$ Eq. (26)
  Update $\tilde{\mathbf{M}}_{n+1}, \tilde{\mathbf{f}}_{n+1}$ Eq. (7)
  Update $\mathbf{c}_{\text{N}n+1}$ and $\mathbf{c}_{\text{N}\Lambda n+1}$ Eq.Eq. (49), Eq.Eq. (53)
end while

This value corresponds to the pin abscissa where the temperature reaches 1% of the surface temperature [42] in the case of linear transient heat equation with semi-infinite solid. Figure 4 shows the evolution of the element size for the mesh used. Its thermal behaviour has been validated with a transient non linear heat conduction problem. The pin is assumed to be initially at 298 K and submitted to a constant heat power of $23 \cdot 10^3$ W during 10 ms. It allows to cover the whole interpolation range of temperature. Material properties are those from [33], with $C_{\text{p}} \in [425, 634]$ J·kg^{-1}·K^{-1} and $\lambda_{\text{pin}} \in [9.94, 25.32]$ W·m^{-1}·K^{-1}. Figure 5 shows well correlation between results from the developed model and Ansys with less than 2% error. Also, the three first traction-compression eigenvalues of the pin have been compared with the ones provided in [43]. With the chosen mesh, the theoretical frequencies are estimated with less than 2% error.

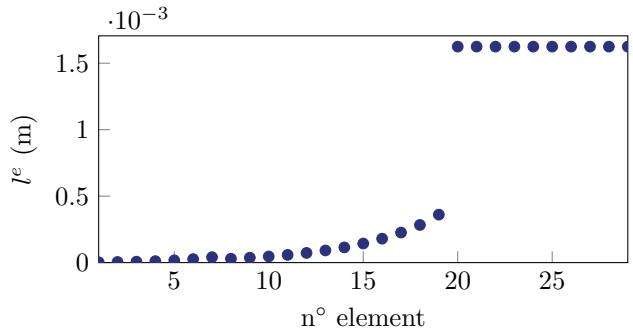

Figure 4. Elements size of the pin's mesh.

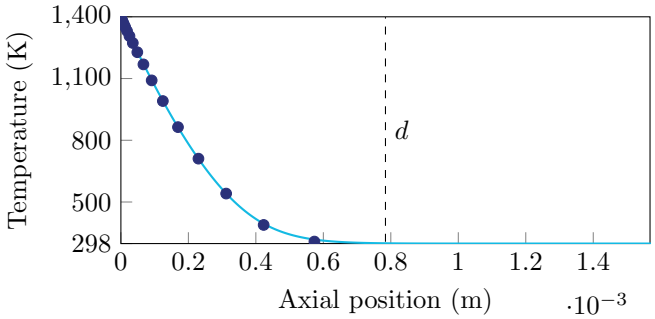

Figure 5. Temperature field in the pin near the contacting surface at $t = 10\,\text{ms}$, Ansys (—), Developed method (●), Distance d (Eq. (54)) at which the mesh becomes uniform (- -).

6 Results

Different analyses are now conducted for the pin-disk configurations. Firstly, the complete dynamics of the test case is evaluated. The contact behavior and the motion of the system are thoroughly analyzed. Simulations were carried out with a time step $\mathrm{d}t = 2 \cdot 10^{-7}\,\text{s}$ so that the first ten modes of the pin are well described. The $\theta-$method is here employed with $\theta = 0.5$ so that the scheme is implicit without additional numerical damping. The parameters m, j, p for the computation of the disk temperature are respectively set to 25, 25, 250 (see Eq. (41)). Secondly, the influence of the thermal modeling on the system response is investigated.

6.1 Global dynamic response

The computed transient response accounts for time changing rotating speed and adhesive wear. Also, the non linear heat behavior of the pin and its thermal expansion are included. Finally, heat loss by convection and a heat partitioning dependent on the material properties are also considered.

Results are displayed on Fig.6 . Two distinct phases can be observed from Fig.6a. The first part of the interaction consists of impacts while the second is characterized by permanent contact. During phase 1, the amplitude of the impacts rapidly decay from 350 µm to less than 10 µm. Furthermore as a consequence of impacts, the load seen by the pin is far larger than the external load applied at the rotor disk level. With the chosen configuration, the pin undergoes a load almost sixty times greater than $\mathbf{F}_{\text{aer}}$. Thus, the heat flux generated at the interface is higher than during permanent contact (Fig.6c, Fig.10b). From Fig.6c it can be seen that the heat penetration is lower during the first part of the interaction than during the second one, which is due to the short contacting time caused by impacts.

Accounting for the full dynamics of the rotor has been shown to have an important influence on the transient response. Indeed, the impact dynamics induces the fusion of the pin interface with an external load for which the

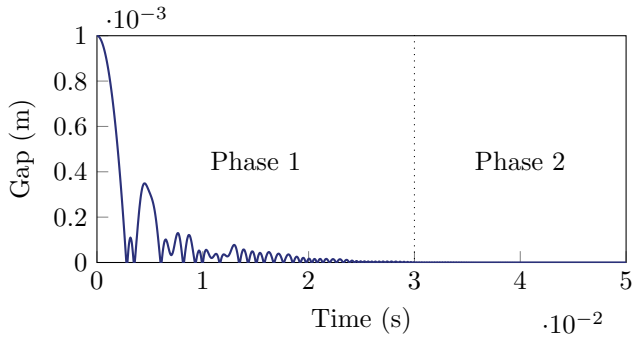

(a) Gap with time

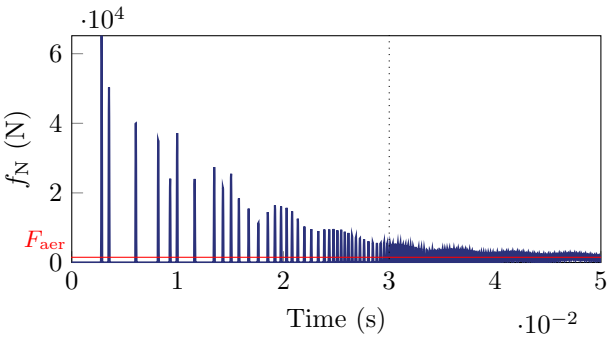

(b) Reaction with time

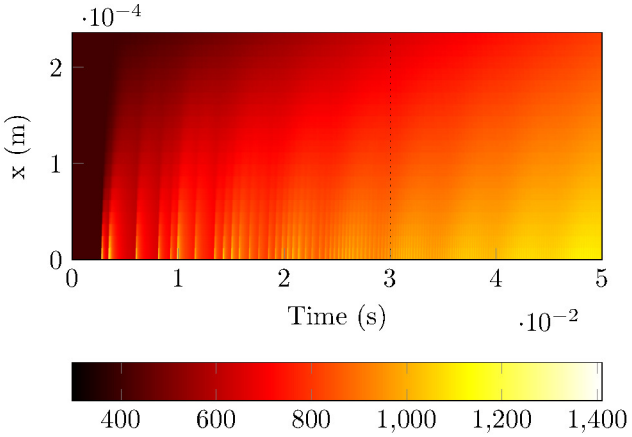

(c) Heat penetration in the pin with time

Figure 6. Gap, reaction force and temperature in the pin.

fusion does not occur when permanent contact is assumed. Moreover, in case of a larger gap or a greater $\mathbf{F}_{\text{aer}}$, the pin is likely to locally plastify which may not happen with permanent contact hypothesis.

The temperature on the surface of the disk at a radius $r = r_{\text{pin}}$ is displayed on Fig.7. The center of the pin is assumed to be located at $\theta_{\text{disk}} = 0$ and the dotted lines delimit the contact area. From Fig.7, it can be seen that the temperature of the disk starts increasing as soon as entering the contact area. The maximum temperature at the disk surface is obtained at the exit of the contact area. As the time between two contact phases decreases, the disk's surface accumulates heat and enters the contact area at a higher temperature. As a consequence, the part of heat that goes to the pin slowly decreases as the disk is heated.

Rotor's dynamic is displayed on Fig.8. Its rotations and translations at point G along $\overrightarrow{Y}, \overrightarrow{Z}$ are displayed in Figures 8a, 8b. The first two suspension modes of the system are found within the rotor displacements in the plan $(\overrightarrow{\text{Y}}, \overrightarrow{\text{Z}})$. During phase 2, the rotor rotates with a frequency that corresponds to its first suspension mode.

The braking effect of the pin on the rotor disk is visible in Fig.8c. It shows that the rotation speed of the rotor is slowed down and the time needed to reach Ω_{lim} is here delayed by $\gamma_t = 11.7\,\text{ms}$.

The pin shortening due to adhesive wear is provided on Fig.9 . According to Eq. (22), the wear depth strongly increases while permanent contact is reached. However, in case of short event, adhesive wear does not have a significant influence. Indeed, compared to the thermal expansion of the pin which is in the range of micrometers (Fig.11) the wear depth is in the range of the nanometer.

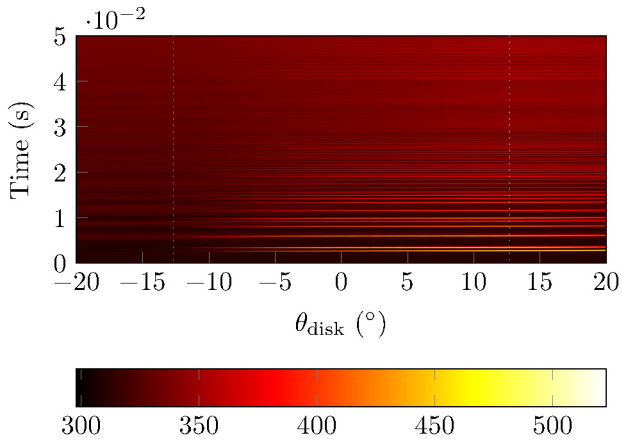

Figure 7. Temperature (K) at the disk surface at $r = r_{\text{pin}}$, the heat source is located at 0°, limits of the contact area (····).

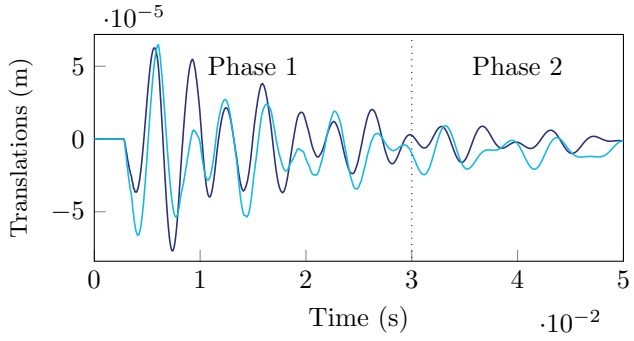

(a) Translations, (Y axis (——), Z axis (——)).

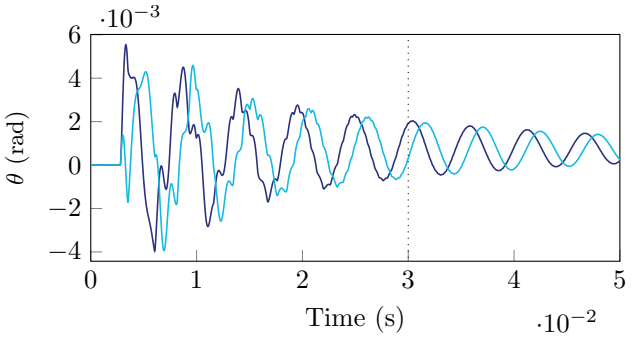

(b) Rotations, (Y axis (——), Z axis (——)).

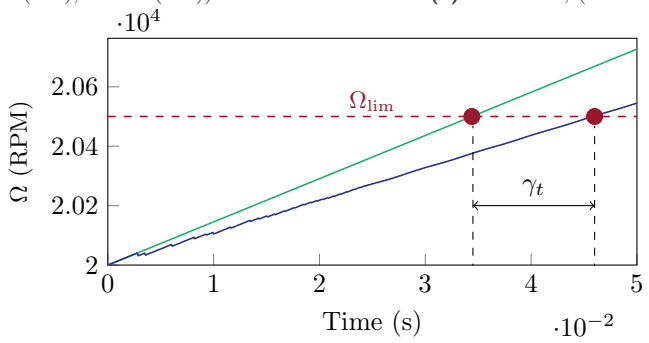

(c) Ω with time, (pin-Disk interaction (——), Free response (——)).

Figure 8. Rotor dynamics at point G

6.2 Impact of thermal modeling

In order to investigate the influence of the thermal phenomenon considered in the present methodology, five configurations have been studied. Configurations 1 corresponds to the full system presented in Sec.4.1. The other configurations are different from the reference case through a single modification. The second configuration does not account for temperature dependent material properties. The third configuration assumes that the heat flow is equally shared during the whole interaction. The thermal expansion is not considered in the fourth configuration. The fifth and last configuration ignores the temperature and just solves the mechanics part of the system.

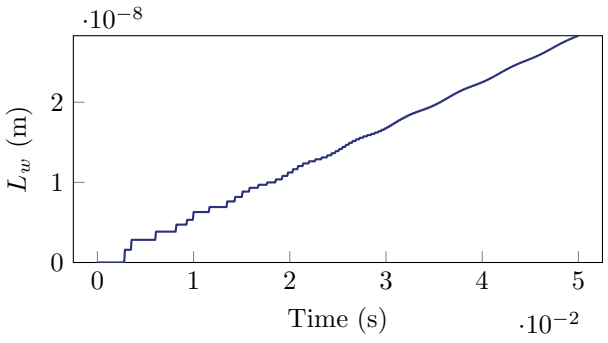

Figure 9. Wear depth

Firstly, the temperature evolution at the pin surface is compared between the first three configurations. The results are provided in Fig.10. The red line represents the melting temperature (T_{melt}) which is 1400 K for the selected material. With Configuration 2, T_{melt} is exceeded even during permanent contact whereas it is kept below 1400 K for configuration 1 and 3. As shown on Fig.10a, non linear heat modeling allows a better diffusion of heat within the body avoiding heat accumulation at the surface leading to a lower surface temperature. Also, comparing Configuration 3 with Configuration 1 shows that the pin tends to absorb more heat during the contact process. Compared to Configuration 1, the maximum absolute difference is 670 K for Configuration 2 and 213 K for Configuration 3. Thus, non linear heat modelling has a first order impact on the thermal response of the pin which is consistent with the result from [4] . Also material dependent heat partition ratio significantly influences the temperature at the pin surface. Thus, they are both key parameters in order to accurately model the present interaction. It should be noted that the rate of temperature increase obtained in the present paper is somehow overestimated as the friction coefficient μ is considered constant.

In order to assess the influence of the pin's temperature on the system dynamic response, the gap and the pin's

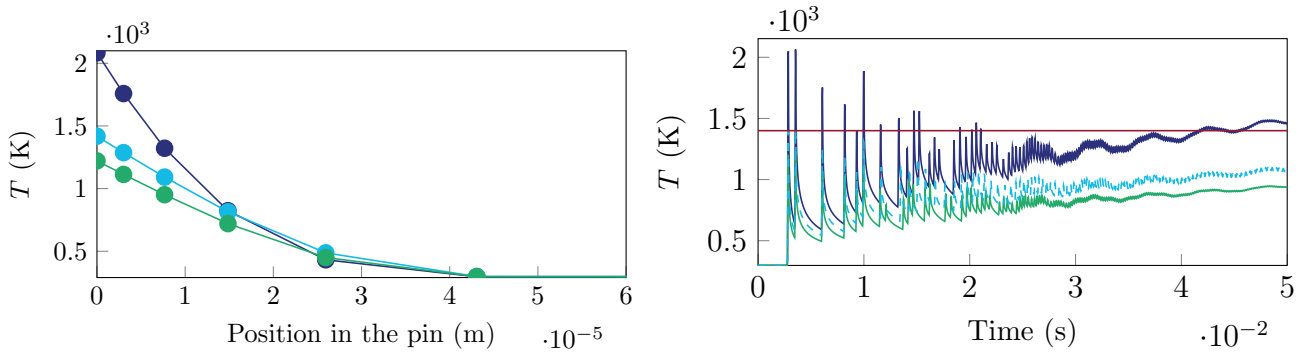

(a) Heat penetration at first impact

(b) Temperature at pin's surface

Figure 10. Temperature in the pin, Configuration 1 (—), Configuration 2 (—), Configuration 3 (—).

displacement obtained with Configuration 2, 4 and 5 were compared, results are presented in Fig.11. Doing so allows to decouple the influence of thermal expansion and thermal softening. The change in Young's modulus of the material near the pin surface has a damping effect on the transient response of the system. Indeed, the gap closes ≈ 5 ms earlier with Configuration 4 than with Configuration 5 (see Fig.11a). Also, the amplitude of the pin oscillations decreases faster with Configuration 4 so much that only the first normal mode of the rotor remains at 50 ms with a small amplitude (see Fig.11b).

Thermal expansion (Configuration 2) also affects the dynamic response of the system and has a destabilizing role by

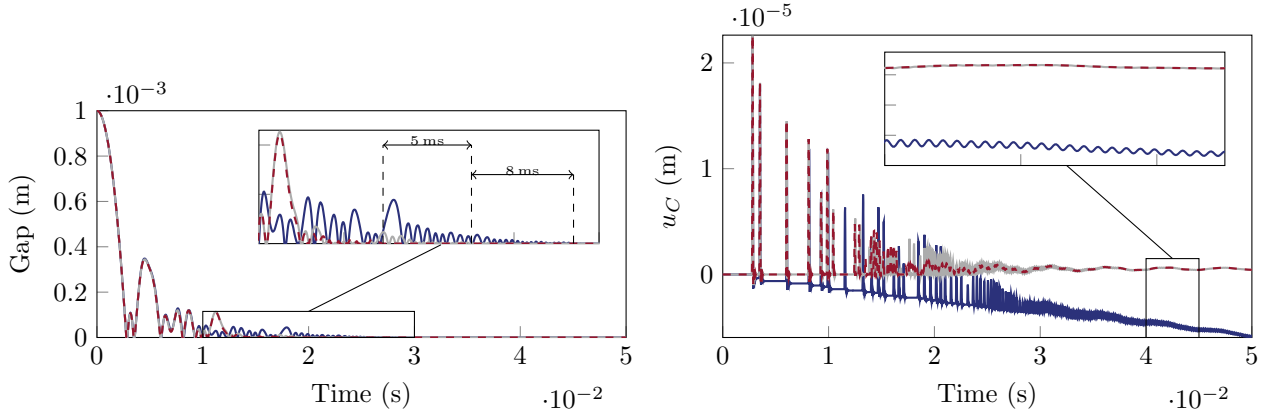

(a) Gap evolution

(b) Displacement of point C with time

Figure 11. Gap and axial translation of the extremity of the pin, Configuration 2 (——), Configuration 4 (- -), Configuration 5 (——).

increasing the number of impacts. Indeed, with Configuration 2 the permanent contact stage is delayed of 8 ms compared with Configuration 5 (see Fig.11a) and the system oscillates faster and with a larger amplitude (see Fig.11b).

7 Conclusion

In this paper, a novel methodology to model braking interaction at high speeds has been proposed. This method relies on the Moreau-Jean algorithm to handle non-smooth and non linear dynamics. This algorithm is improved to account for thermal expansion, material dependence on the temperature, and adhesive wear. As an application, a pin-disk test case has been studied. First, it has been shown that the presence of impacts has an important influence on the response of the system. Indeed, it leads to an increase of the stress in the pin, and thus has a major influence on the heat flux generated at the interface. It has been shown that for a gap of 1 mm, the load seen by the pin is far greater than the one applied at the disk level and that interface melting is very likely to occur before permanent contact arises.

Another major phenomena influencing the dynamics of the test case is the thermal behavior with the non linear heat equation. Indeed accounting for this behavior allow to better predict the time to reach melting by allowing a better diffusion of the heat through the pin. Also, accounting for change in Young's modulus has shown to damp the dynamics and allows to reach permanent contact earlier.

The novelty of the present methodology relies on its capacity to model the transient non linear interaction between a rotor and stator with semi-analytical modelling. Compared to previous studies [2, 3, 4], computational cost is reduced and new physics can easily be added in the modelling. Also, in a future work the proposed methodology will aim to handle impacts, permanent contact with dry friction and permanent contact with melted interface.

From an academic point of view, this methodology is relevant to better understand the phenomenology of braking under severe conditions. Furthermore, this method can be applied in an industrial context at a preliminary stage to evaluate initial designs within a short amount of time. It is also very interesting to assess which physical phenomena are predominant.

As shown in this paper, for some set of parameters (initial load, initial rotating speed and so on), the melting of the pin interface can occur at early stages of contact interaction. This behaviour is not handled yet by the proposed methodology. Moreover, results showed that because of impacts, the loading acting on the pin can reach high values. Therefore, the pin is likely to undergo plasticity. Thus, future works will aim to model plasticity and melting behaviours. Also, implementing multiple pins in contact with the disk would make the studied configuration more realistic.

Acknowledgement

The authors are thankful for the financial support of the ANR (project ANR-22-CPJ2-0061-01) and the HE-ART grant project (ID: 101102013)

A Convective coefficient h

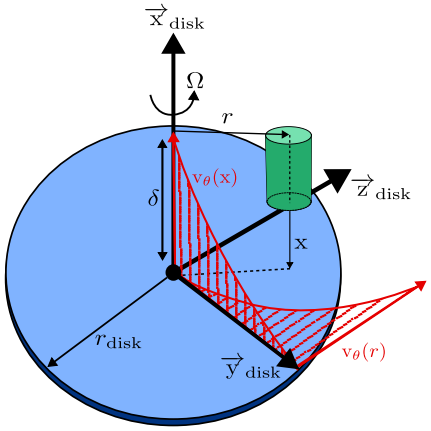

Figure S1. Rotor disk boundary layer interaction with the pin.

The air surrounding the system is assumed to be displaced only by the rotation of the disk. Therefore, out of the boundary layer the fluid is at rest. The turbulent boundary layer is expressed [44] (Eq.4.187) through

$$\delta = 0.5261 r \left(\frac{\nu}{r^2\Omega}\right)^{\frac{1}{5}}, \tag{55}$$

r is the radial position of the pin (Fig.S1) and ν the kinematic viscosity ($\mathrm{m^2{\cdot}s^{-1}}$) computed using Sutherland law. Air velocity in the boundary layer is mainly tangential and expressed [44] (Eq.4.97) by

$$v_\theta = r\Omega \left[1 - \left(\frac{x}{\delta}\right)\right]^{\frac{1}{7}}, \tag{56}$$

x is the axial distance from the disk. Churchill and Bernstein [45] obtained an empirical formula to compute the Nusselt number (Nu) in case of a cylinder perpendicular to an air flow

$$N_u = 0.3 + \left[\frac{0.62 R_e^{\frac{1}{2}} P_r^{\frac{1}{3}}}{\left(1 + \left(\frac{0.4}{P_r}\right)^{\frac{2}{3}}\right)^{\frac{1}{4}}} \left[1 + \left(\frac{R_e}{282000}\right)\right]^{\frac{4}{5}}\right], \tag{57}$$

it is valid for $R_e \leq 10^7$ and $P_r R_e \geq 0.2$. In the previous expression R_e is the Reynold number ($\frac{v_\theta d_{\text{pin}}}{\nu}$) and P_r the Prandtl number (≈ 0.7). For the disk, the mean Nusselt number $\overline{\text{Nu}}$ is used and it is defined in case of an isothermal disk [46, 47]

$$\overline{\text{Nu}} = 0.015 \overline{R_e}^{0.8}, \tag{58}$$

with $\overline{R_e} = \dfrac{\Omega {r_{\text{disk}}}^2}{\nu}$. The convective heat transfer coefficient of the disk and the pin is thus computed

$$\begin{cases} h_{\text{pin}}(x, r, \Omega) = \dfrac{\text{Nu}(x, r, \Omega)\lambda_{\text{air}}(T)}{2r_{\text{pin}}}, \\ \overline{h_{\text{disk}}}(\Omega) = \dfrac{\overline{\text{Nu}}(\Omega)\lambda_{\text{air}}(T)}{r_{\text{disk}}}, \end{cases} \tag{59}$$

λ_{air} is the thermal conductivity of air obtained from [48].

References

[1] C. Jacobs, M. Legrand, F. Thouverez, and P. Almeida. "Turbomachinery transient dynamics of radial rotor-stator contact occurrences with friction". *Proceedings of GT 2023*. Vol. 87066. 2023, V11BT26A007.

[2] A. Psarra. "Gas turbine shaft failure modelling friction and wear modelling of turbines in contact". PhD thesis. Cranfield University, 2010.

[3] P. Capozzi, A. Psarra, V. Pachidis, and P. Pilidis. "A Finite Element Approach of Turbines in Contact Following a Shaft Failure Event". *Volume 3: Controls, Diagnostics and Instrumentation; Cycle Innovations; Marine*. ASME Turbo Expo 2010: Power for Land, Sea, and Air. 2010, pp. 813–820. DOI: 10.1115/GT2010-23298.

[4] I. Rojo, A. Psarra, V. Pachidis, and P. Pilidis. "Evaluation of the Energy Dissipated as Friction/Heat Between Turbines Following Shaft Failure". *Volume 6: Structures and Dynamics, Parts A and B*. ASME Turbo Expo 2010: Power for Land, Sea, and Air. 2010, pp. 1345–1352. DOI: 10.1115/GT2010-23302.

[5] I. Eryilmaz and V. Pachidis. "Turbine thermomechanical modelling during excessive axial movement and overspeed". The Aeronautical Journal Vol. 123 (2019), pp. 248–264. DOI: 10.1017/aer.2018.162.

[6] V. Acary and B. Brogliato. Numerical methods for nonsmooth dynamical systems: applications in mechanics and electronics. 2008. DOI: 10.1007/978-3-540-75392-6.

[7] S. Lim and M. Ashby. "Overview no. 55 Wear-Mechanism maps". Acta Metallurgica Vol. 35 (1987), pp. 1–24. DOI: 10.1016/0001-6160(87)90209-4.

[8] R. Montgomery. "Friction and wear at high sliding speeds". Wear Vol. 36 (1976), pp. 275–298. DOI: 10.1016/0043-1648(76)90108-3.

[9] T. A. Laursen. Computational Contact and Impact Mechanics Fundamentals of Modeling Interfacial Phenomena in Nonlinear Finite Element Analysis.

[10] P. Wriggers and T. A. Laursen. Computational contact mechanics. Vol. 2. 2006. DOI: 10.1007/978-3-540-32609-0.

[11] H. Meng and K. Ludema. "Wear models and predictive equations: their form and content". Wear Vol. 181-183 (1995), pp. 443–457. DOI: 10.1016/0043-1648(95)90158-2.

[12] S. Fouvry, T. Liskiewicz, P. Kapsa, S. Hannel, and E. Sauger. "An energy description of wear mechanisms and its applications to oscillating sliding contacts". Wear Vol. 255 (2003), pp. 287–298. DOI: 10.1016/S0043-1648(03)00117-0.

[13] H.Blok. "Les Températures de Surface dans des Conditions de Graissage Sous Extrême Pression". Proc. Sd. World Petrol. Cong., vol. 3 (1937).

[14] J. C. Jaeger. "Moving sources of heat and the temperature at sliding contacts". J. Proc. - R. Soc. N. S. W. (1943). DOI: 10.5962/p.360338.

[15] J. F. Archard. "The temperature of rubbing surfaces". Wear Vol. 2 (1959), pp. 438–455. DOI: 10.1016/0043-1648(59)90159-0.

[16] J. Barber. "Distribution of heat between sliding surfaces". J. Mech. Eng. Sci. Vol. 9 (1967), pp. 351–354. DOI: 10.1243/JMES_JOUR_1967_009_054_02.

[17] F.Charron and P.Vernotte. Partage de la chaleur entre deux corps frottants. 1943.

[18] A. Yevtushenko, K. Topczewska, and P. Zamojski. "The Heat Partition Ratio during Braking in a Functionally Graded Friction Couple". Materials Vol. 15 (2022). DOI: 10.3390/ma15134623.

[19] M. K. Mondal, K. Biswas, and J. Maity. "A transient heat transfer model for assessment of flash temperature during dry sliding wear in a pin-on-disk tribometer". Metall. Mater. Trans. Vol. 47 (2016), pp. 600–607. DOI: 10.1007/s11661-015-3224-6.

[20] H. Carslaw and J. Jaeger. Conduction of Heat in Solids. Oxford, 1959.

[21] J. J. Moreau. "Unilateral contact and dry friction in finite freedom dynamics". *Nonsmooth mechanics and Applications*. 1988, pp. 1–82.

[22] M. Jean. "The non-smooth contact dynamics method". Comput. Methods Appl. Mech. Eng. Vol. 177, No. 3-4 (1999), pp. 235–257. DOI: 10.1016/S0045-7825(98)00383-1.

[23] V. Acary. "Projected event-capturing time-stepping schemes for nonsmooth mechanical systems with unilateral contact and Coulomb's friction". Comput. Methods Appl. Mech. Eng. Vol. 256 (2013), pp. 224–250. DOI: 10.1016/j.cma.2012.12.012.

[24] P. Almeida, C. Gibert, F. Thouverez, X. Leblanc, and J.-P Ousty. "Numerical analysis of bladed disk - casing contact with friction". J. Eng. Gas Turbine. Power Vol. 138 (2016). DOI: 10.1115/1.4033065.

[25] F. Bowden and D Tabor. The Friction and Lubrication of Solids, Part I, Clarendon. 1950.

[26] M. Jahangiri, M. Hashempour, H. Razavizadeh, and H. Rezaie. "A new method to investigate the sliding wear behaviour of materials based on energy dissipation: W–25wtCu composite". Wear Vol. 274-275 (2012), pp. 175–182. DOI: 10.1016/j.wear.2011.08.023.

[27] N. Strömberg, L. Johansson, and A. Klarbring. "Derivation and analysis of a generalized standard model for contact, friction and wear". Int J. Solids Struct. Vol. 33 (1996), pp. 1817–1836. DOI: 10.1016/0020-7683(95)00140-9.

[28] J. P. Bardon. "Bases physiques des conditions de contact thermique imparfait entre milieux en glissement relatif". Revue Générale de Thermique Vol. 33 (1994).

[29] R. Dou, T. Ge, X. Liu, and Z. Wen. "Effects of contact pressure, interface temperature, and surface roughness on thermal contact conductance between stainless steel surfaces under atmosphere condition". International Journal of Heat and Mass Transfer (2016). DOI: 10.1016/j.ijheatmasstransfer.2015.11.069.

[30] N Laraqi. "Phenomene de constriction thermique dans les contacts glissants". Int. J. Heat Mass Transfer (1996). DOI: 10.1016/0017-9310(95)00395-9.

[31] J. Vullierme, J. Lagarde, and H. Cordier. "Etude de la resistance de contact entre deux materiaux en frottement—Influence de la vitesse relative de glissement". International Journal of Heat and Mass Transfer (1979). DOI: 10.1016/0017-9310(79)90167-4.

[32] J. Barber. "The conduction of heat from sliding solids". Int. J. Heat Mass Transf. Vol. 13 (1970), pp. 857–869. DOI: 10.1016/0017-9310(70)90131-6.

[33] A. S. Agazhanov, D. Samoshkin, and Y. M. Kozlovskii. "Thermophysical properties of Inconel 718 alloy". *Journal of Physics: Conference Series*. Vol. 1382. IOP Publishing. 2019, p. 012175.

[34] R. Akamatsu, T.-T. Ikeshoji, M. Araki, M. Yonehara, K. Namamura, and H. Kyogoku. "Numerical analysis of thermal deformation and residual stress for selective laser melting process". AIP Conf Proc (2016). DOI: 10.1299/jsmemp.2016.24.431.

[35] C. Li, R. Karimbaev, S. Wang, A. Amanov, D. Wang, and M. Abdel Wahab. "Fretting wear behavior of Inconel 718 alloy manufactured by DED and treated by UNSM". Scientific Reports Vol. 13 (2023), p. 1308. DOI: 10.1038/s41598-023-28128-8.

[36] L.-W. Chen and D.-M. Ku. "Dynamic stability of a cantilever shaft-disk system". J. Vib. Acoust. (1992). DOI: 10.1115/1.2930265.

[37] G. Cowper. "The shear coefficient in Timoshenko's beam theory". J. Appl. Mech. Vol. 33 (1966), pp. 335–340. DOI: 10.1115/1.3625046.

[38] A. J. M. Arizmendi F. Veiga and A. G. D. Val. "Transient temperature distribution in a rotating cylinder subject to a surface heat source and convective cooling". Numer. Heat Transf. A Vol. 82 (2022), pp. 743–764. DOI: 10.1080/10407782.2022.2083869.

[39] N. Laraqi, N. Alilat, J. G. de Maria, and A. Baïri. "Temperature and division of heat in a pin-on-disc frictional device—Exact analytical solution". Wear Vol. 266 (2009), pp. 765–770. DOI: 10.1016/j.wear.2008.08.016.

[40] D. W. Hahn and M. N. Özisik. Heat conduction. 2012. DOI: 10.1002/9781118411285.

[41] A. B. Nacim Alilat and N. Laraqi. "Three dimensional calculation of temperature in a rotating disk subjected to an eccentric circular heat source and surface cooling". Numer. Heat Transf. A Vol. 46 (2004), pp. 167–180. DOI: 10.1080/10407780490463485.

[42] X. T. Yan. "On the Penetration Depth in Fourier Heat Conduction". Joint Thermophysics and Heat Transfer Conference ().

[43] M. Géradin and D. J. Rixen. Mechanical vibrations: theory and application to structural dynamics. 2014.

[44] P. Childs. Rotating flow. 2010. DOI: 978-0-12-382098-3.

[45] S. W. Churchill and M. Bernstein. "A Correlating Equation for Forced Convection From Gases and Liquids to a Circular Cylinder in Crossflow". J. Heat Transfer Vol. 99 (1977), pp. 300–306. DOI: 10.1115/1.3450685.

[46] I. Shevchuk. "Turbulent Heat Transfer of Rotating Disk at Constant Temperature or Density of Heat Flux to the Wall". High Temperature Vol. 38 (2000), pp. 499–501. DOI: 10.1007/BF02756017.

[47] S. aus der Wiesche. "Heat transfer from a rotating disk in a parallel air crossflow". Int. J. Therm. Sci. Vol. 46 (2007), pp. 745–754. DOI: 10.1016/j.ijthermalsci.2006.10.013.

[48] K. Stephan and A Laesecke. "The thermal conductivity of fluid air". J. Phys. Chem. Ref. Vol. 14 (1985), pp. 227–234. DOI: 10.1063/1.555749.